Time Domain Astrophysics — 2020/21 — Data Exercise

1 Introduction & Aims

The primary aim of this exercise is to analyse the evolution of a classical nova using photometry and spectroscopy. Using these two tools, we wish to classify the nova in terms of its light-curve and speed class. Combining the information, we eventually try to estimate the distance to this nova. The methods, results and analysis are discussed for photometry in section 2.1 and for spectroscopy in section 2.2. Discussions and conclusions are also presented alongside the presentation of related results in the same section 2, followed by a list of references.

2 Methods, Results & Analysis

2.1 Photometry

Photometry of the nova is performed using the GAIA software which is a part of Starlink suite of software applications. The images when viewed in software initially provide little or no information with few white dots on a dark background. To help with extracting information from the images, the *auto cut, colour map, intensity map* and *colour bar* features are used according to the requirements. The *auto cut* feature, which is sufficient in most cases, varies the data limits on brightest and faintest object in the image. A value of 98-99.5% is optimum for most images. The other three features are used to vary the number, scale and palette of image colours, which may help in providing a better visualization.

In order to perform the photometry, the basic necessity is to first successfully locate the nova in the provided series of 18 SDSS *r'*-band photographic images obtained using Liverpool Telescope. For this, the images are compared and the object whose brightness varies (eventually fades) over time is identified at position $(1055, 978)$ on every image grid, which corresponds to right ascention and declination of the object at roughly $\alpha = 00:44:41.05$ and $\delta = 40:08:36.00$, respectively.

The format of the images file is called *FITS* - Flexible Image Transport System. It consists of two sections – *image header* followed by *image data*. The header provides a lot of information about the image, a few of which, like the DATE-OBS (date/time of observation), MJD (modified Julian date), EXPTIME (exposure time), GAIN (photoelectrons per data unit) and AIRMASS (relative optical path length through atmosphere) are noted, for further use in performing photometry. The EXPTIME for initial sixteen images (phot_00.fits – phot_15.fits) is 120 seconds, while for the final two images (phot_16.fits and phot_17.fits) the value is 300 seconds. The value of GAIN for each image is noted to be 1.62 photoelectrons per data unit.

For each image, point spread function (PSF) of the nova is observed, and the its span along x-axis in units of number of pixels is noted and summarized in table 1. The value for image phot_11.fits could not be obtained given that the nova in the image could not be located with enough confidence possibly due to poor photometric conditions. It can be seen that, in general, the span is seen to roughly decrease over time and remains roughly constant in the final images, where exposure time is increased. This trend can be attributed to possible two effects – change in viewed psf of nova and variation in sky (background) brightness. Our estimates of the same are also biased by the value of differing values of auto cut used in different images. Therefore, decrease in span can be attributed most prominently to reducing PSF of the nova.

To perform the approximate photometry, the *Aperture Photometry in magnitudes* option is used first. For this, we use a frame zero point of 0 magnitudes and input the values of exposure time and gain for the image being analysed. Image of a faint object captured over long exposure time may be brighter than the image of a bright object captured over smaller exposure time. Similarly, high gain would require more photons per data unit. Therefore, our perception of bright and faint objects may vary from one image to another with varying exposure times and gains. Hence, it is important to account for both of these parameters for each image.

Once these values are entered, a circular aperture is defined over the nova with surrounding annulus used for estimating background noise. A very small aperture would lead to loss of signal by discarding useful

file	x-axis span	aperture
phot_00.fits	1049–1061	7.0
phot_01.fits	1049–1061	6.5
phot_02.fits	1049–1061	5.5
phot_03.fits	1050–1061	5.4
phot_04.fits	1052–1058	4.9
phot_05.fits	1053–1058	4.9
phot_06.fits	1052–1058	8.0
phot_07.fits	1053–1058	4.4
phot_08.fits	1050–1060	7.5
phot_09.fits	1053–1058	4.6
phot_10.fits	1053–1058	3.1
phot_11.fits	–	4.4
phot_12.fits	1053–1057	3.6
phot_13.fits	1054–1057	2.5
phot_14.fits	1054–1057	2.3
phot_15.fits	1054–1056	4.2
phot_16.fits	1053–1056	3.3
phot_17.fits	1054–1056	2.9

Table 1: The span of PSF of the nova across x-axis, in units of pixels range, and the size (semi-major-axis) of optimal aperture, in units of number of pixels, calculated for different photometric image files.

signal. A large aperture would include a lot of noise. Hence in both cases, signal to noise ratio is decreased, although in different manners. An optimal aperture considers all the signal while discarding maximum possible noise. The value of estimated background noise from the annulus is subtracted from the value obtained from aperture (which contains both signal from nova and noise) to obtain true signal. Consequently, the most optimal aperture is the one with maximum signal as well as highest signal-to-noise ratio.

Upon performing photometry for different combinations of aperture and annulus radii, it is observed that the errors are not statistical, but instead depend upon the radius of the aperture used. Both small and large apertures are inefficient and an optimum aperture lies in between that range.

To estimate an optimal aperture size for an image, *Aperture Photometry using data counts* option is used. For a range of values of aperture sizes, the values of mean counts, error in counts and signal-to-noise ratios (SNR) are noted. For image phot_00.fits, the variation in SNR with aperture size is shown in figure 1a. It should be noted that the value of aperture size calculated for an image should be retained across all measurements performed using that image. This is to make sure that we account for the same ratio of light received from each object in the image and therefore, consistent relative values of brightness are obtained.

Using the same procedure, values of optimal apertures for each image can be calculated and are summarized in table 1. These values vary for different images depending upon several factors like atmospheric seeing (or the background noise), object brightness, exposure time, etc.

To obtain photometric measurements for the nova, we need to compare its brightness to that of standard stars, whose true photometric measurements, under *idealized* conditions are already known and publicly available in catalogs. Accordingly, five secondary standards stars, given their availability in our field of view, are selected to calibrate our photometry of nova. Their IDs in the catalog provided, along with their corresponding approximate positional coordinates on image grid are given in table 2. We need to consider only the stars which have been observed to remain static (i.e. not a variable star) over extremely long periods, so that its low photometric uncertainty can be considered reliable for calibration. Even if the atmospheric seeing is unfavourable, photometry can still be performed if we can safely assume that the extent of unfavourability of conditions is similar for both the objects (– nova being studied and the standard star), which is a reasonable assumption

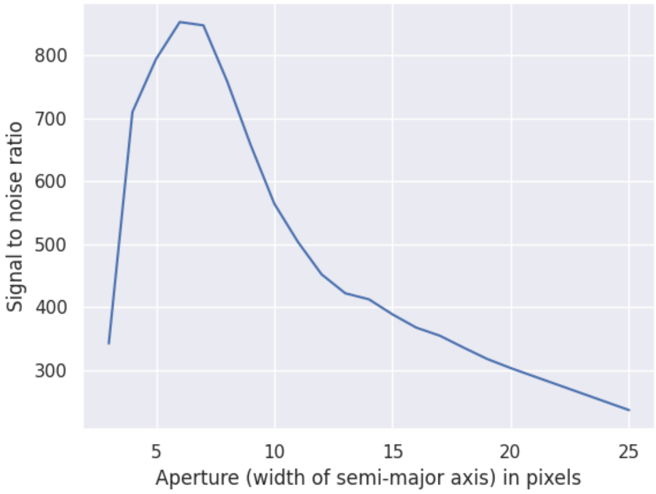

(a) Variation of signal-to-noise ratio with aperture size for the nova in first photometric image file phot_00.fits. For each entry, inner and outer radii of annulus are $r_a = 1.5$ pixels and $r_b = 2.0$ pixels respectively.

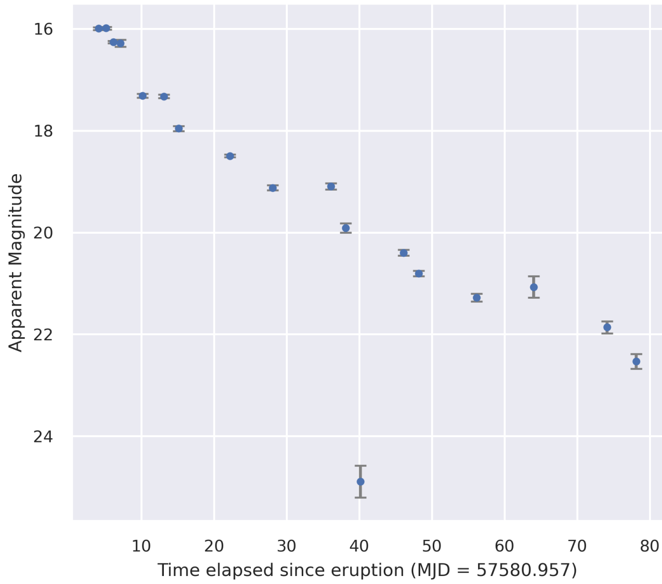

(b) The calculated r'-band light curve for the nova.

Figure 1: Plot used for estimation of optimal aperture size for image and the light curve of the nova.

Star	Catalog ID	Position	r	r error	g	g error	r'
Star 1	11	(1079,741)	16.1868	0.0044	16.8984	0.0052	16.194
Star 2	2	(985,665)	16.7696	0.0065	17.5087	0.0059	16.777
Star 3	6	(740,1205)	16.5210	0.0066	16.9415	0.0034	16.525
Star 4	30	(392,1111)	18.1143	0.0062	18.5278	0.0049	18.118
Star 5	10	(1275,1305)	15.7283	0.0020	16.0337	0.0042	15.731

Table 2: PS1 catalog IDs and approximate positional coordinates of secondary standards used for calibrating photometry of nova.

for the nearby secondary standards. Secondly, slightly distant secondary stars in the field of view can be used to estimate variabilities in atmospheric extinction across field of view. For observing faint events, exposure times are often long enough to primary standards. Somewhat dimmer secondary standards are therefore more helpful in these cases.

A large number of PS1 secondary standard stars are available in field of view. However, not all of them are suitable enough to be used in our case. Parameters like vicinity to the nova and brightness comparable to that of our nova help in selection of most suitable standard stars. Vicinity leads to correlating atmospheric extinction for the two objects. Comparable brightness or *spread* of stars aids the use of same aperture for all standard stars as well as the nova in the image. It must be noted that every secondary star selected should be capable of being resolved properly in the images.

Equipped with the procedure followed so far, we can obtain photometry of nova as well as the five secondary standards. The obtained apparent magnitudes (m_{nova} and m_{star}) are given in table 3.

In order to use the photometric measurements provided in the PS1 catalog, we need to translate values presented in PS1 system to SDSS system as mentioned in the handout. This conversion is performed in table 2 using the relation (Tonry et al., 2012):

$$r' = r - 0.001 + 0.11(g - r) \pm 0.004 \tag{1}$$

Now, we use the following equation to obtain values of zero-point for each observation, given by Z in the following equation. The values computed are given in table 4.

$$Z = r' - m_{star} \tag{2}$$

Nova	Star 1	Star 2	Star 3	Star 4	Star 5
-8.069 ± 0.006	-8.792 ± 0.003	-8.193 ± 0.005	-8.432 ± 0.004	-6.820 ± 0.016	-9.235 ± 0.002
-8.118 ± 0.005	-9.086 ± 0.002	-8.492 ± 0.004	-8.727 ± 0.003	-7.117 ± 0.011	-9.522 ± 0.002
-7.788 ± 0.007	-8.949 ± 0.003	-8.348 ± 0.004	-8.585 ± 0.003	-6.954 ± 0.013	-9.379 ± 0.002
-7.750 ± 0.007	-9.066 ± 0.002	-8.472 ± 0.004	-8.710 ± 0.003	-7.093 ± 0.125	-9.510 ± 0.001
-7.014 ± 0.016	-8.672 ± 0.004	-8.078 ± 0.006	-8.330 ± 0.005	-6.729 ± 0.020	-9.109 ± 0.003
-6.795 ± 0.016	-8.761 ± 0.003	-8.170 ± 0.005	-8.411 ± 0.004	-6.801 ± 0.016	-9.201 ± 0.002
-6.225 ± 0.026	-8.443 ± 0.003	-7.863 ± 0.006	-8.095 ± 0.005	-6.459 ± 0.021	-8.870 ± 0.003
-6.003 ± 0.010	-8.784 ± 0.002	-8.199 ± 0.003	-8.448 ± 0.002	-6.839 ± 0.006	-9.238 ± 0.002
-5.190 ± 0.031	-8.447 ± 0.003	-7.868 ± 0.004	-8.105 ± 0.003	-6.488 ± 0.010	-8.890 ± 0.002
-5.316 ± 0.046	-9.070 ± 0.002	-8.475 ± 0.003	-8.721 ± 0.003	-7.120 ± 0.009	-9.512 ± 0.002
-4.584 ± 0.072	-8.588 ± 0.003	-8.007 ± 0.004	-8.269 ± 0.003	-6.6333 ± 0.012	-9.035 ± 0.002
0.351 ± 0.284	-7.629 ± 0.007	-7.0654 ± 0.012	-7.293 ± 0.010	-5.638 ± 0.041	-8.089 ± 0.005
-4.087 ± 0.038	-8.717 ± 0.002	-8.138 ± 0.003	-8.385 ± 0.002	-6.775 ± 0.005	-9.163 ± 0.002
-3.757 ± 0.037	-8.403 ± 0.002	-7.811 ± 0.003	-8.072 ± 0.003	-6.452 ± 0.006	-8.851 ± 0.002
-3.280 ± 0.056	-8.462 ± 0.002	-7.897 ± 0.003	-8.153 ± 0.003	-6.525 ± 0.006	-8.933 ± 0.002
-3.371 ± 0.193	-8.819 ± 0.002	-8.214 ± 0.003	-8.463 ± 0.003	-6.862 ± 0.009	-9.251 ± 0.002
-2.690 ± 0.103	-8.512 ± 0.001	-7.917 ± 0.002	-8.173 ± 0.001	-6.534 ± 0.004	-8.959 ± 0.001
-1.997 ± 0.128	-8.089 ± 0.001	-7.494 ± 0.002	-7.763 ± 0.002	-6.098 ± 0.005	-8.518 ± 0.001

Table 3: Values of apparent magnitudes (rounded off to three decimal places) and corresponding error estimates obtained for nova and secondary stars corresponding to the 18 photometric images.

Airmass	Star 1	Star 2	Star 3	Star 4	Star 5
1.7258	24.985 ± 0.007	24.970 ± 0.009	24.956 ± 0.008	24.937 ± 0.020	15.992 ± 0.026
1.6665	25.280 ± 0.006	25.268 ± 0.007	25.251 ± 0.006	25.235 ± 0.015	15.985 ± 0.023
1.7491	25.143 ± 0.006	25.124 ± 0.008	25.109 ± 0.007	25.072 ± 0.017	16.257 ± 0.026
1.7721	25.260 ± 0.006	25.249 ± 0.007	25.234 ± 0.007	25.210 ± 0.129	16.279 ± 0.069
1.3530	24.866 ± 0.007	24.855 ± 0.010	24.854 ± 0.009	24.846 ± 0.024	17.312 ± 0.038
1.6443	24.954 ± 0.007	24.946 ± 0.008	24.936 ± 0.007	24.918 ± 0.019	17.323 ± 0.035
1.5562	24.637 ± 0.007	24.639 ± 0.010	24.619 ± 0.009	24.577 ± 0.025	17.956 ± 0.048
1.1115	24.978 ± 0.005	24.976 ± 0.006	24.972 ± 0.006	24.957 ± 0.009	18.493 ± 0.026
1.3717	24.641 ± 0.006	24.645 ± 0.007	24.630 ± 0.007	24.605 ± 0.014	19.122 ± 0.049
1.2355	25.264 ± 0.006	25.252 ± 0.007	25.245 ± 0.006	25.242 ± 0.013	19.092 ± 0.063
1.1156	24.781 ± 0.006	24.783 ± 0.008	24.793 ± 0.007	24.750 ± 0.015	19.910 ± 0.090
1.0482	23.823 ± 0.011	23.842 ± 0.015	23.818 ± 0.013	23.756 ± 0.044	24.893 ± 0.313
1.1306	24.911 ± 0.005	24.915 ± 0.006	24.910 ± 0.006	24.893 ± 0.009	20.396 ± 0.054
1.0244	24.597 ± 0.006	24.588 ± 0.007	24.597 ± 0.006	24.569 ± 0.010	20.802 ± 0.054
1.0250	24.655 ± 0.006	24.673 ± 0.006	24.677 ± 0.006	24.643 ± 0.009	21.278 ± 0.073
1.1904	25.012 ± 0.006	24.991 ± 0.007	24.988 ± 0.006	24.979 ± 0.012	21.070 ± 0.210
1.0329	24.706 ± 0.005	24.694 ± 0.005	24.697 ± 0.005	24.651 ± 0.008	21.862 ± 0.119
1.0706	24.283 ± 0.005	24.270 ± 0.006	24.287 ± 0.006	24.216 ± 0.009	22.529 ± 0.145

Table 4: Values of airmass and zero-point, Z (given by equation 2), with corresponding error estimates for each of the 18 image files in sequence. Values of Z are truncated to three decimal places for representation.

star	Z at airmass 1	slope
1	24.58518	0.72978
2	24.58542	0.71267
3	24.58767	0.68760
4	24.55271	0.70689
5	24.57150	0.71021

Table 5: Value of Z at airmass 1 and the slope of best fit line to the values of Z for each secondary standard star.

Now, for each star, we use the values of Z from table 4 and find the best fit line for them. Then, we calculate the slope of the best-fit line and evaluate the value of Z at the value of airmass equal to 1. These values for each secondary star are summarised in table 5.

The magnitude of nova obtained using each secondary standard star (m_{nova}^{star}) can now be obtained using the equation,

$$m_{nova}^{star} = Z_{star} + m_{nova} - C_{airmass}, \tag{3}$$

where $C_{airmass}$ is the airmass correction given by,

$$C_{airmass} = (\text{airmass} - 1) \times \text{slope}. \tag{4}$$

Using this methodology, we obtain the magnitude of nova in each image by using a set of five secondary stars. These values obtained using each standard star, are given in table 6. Given that the values obtained at each epoch seem to be roughly similar within the limits of errors and uncertainties, we can be sure that the performed photometry is consistent, and indeed a suitable choice of secondary stars was made. We now use the mean of these values obtained at each epoch to plot the light-curve given in figure 1b.

On the basis of classification of nova light curves by Strope, Schaefer, & Henden (2010) the shape appears to be that of a smooth light curve with no oscillations, flat top, cusp or any signs of dust dip within the ~ 80 days period of observation. Light curve can be represented by a power-law. The extreme variation in photometry around day 11 is probably due to poor photometric conditions and should not be confused for a dust dip because of two reasons – the variation in magnitude is small compared to typical examples of dust-dip light curves and such a dip is not retained on any of the further observations and cannot be such short lived.

Assuming that the peak occurred on approximately the same time as our first observation (which is roughly the brightest observation), we get the approximate value of peak apparent magnitude, $m_0 \approx 16$ at time, $t_0 \approx 4.122$ days post-eruption. Therefore, $t_2 = 10.986$ days $t_3 = 34.30$ days and $m_{15} = 18.25$.

Maximum magnitude rate of decline (MMRD) relationships for V-band magnitudes involving t_2 and t_3 are given as (Downes & Duerbeck, 2000):

$$M_V = (-11.32 \pm 0.44) + (2.55 \pm 0.32) \log t_2, \tag{5}$$

$$M_V = (-11.99 \pm 0.56) + (2.54 \pm 0.35) \log t_3. \tag{6}$$

If we assume that these relations hold approximately true to r'-band absolute magnitudes also (Darnley et al., 2006), we can estimate distance to the nova using the distance modulus equation given by,

$$m_{r'} - M_{r'} = 5 \log d - 5 + A_{r'}, \tag{7}$$

where, $A_{r'}$ is the not yet known extinction correction term and thereby assumed to b equal to 0. Using equation 5, we obtain,

$$M_{r'}^{t_2} \approx -8.663 \pm 0.773$$

Using equation 6, we obtain,

$$M_{r'}^{t_3} \approx -8.090 \pm 1.098$$

From Star 1	From Star 2	From Star 3	From Star 4	From Star 5	Mean
15.986 ± 0.022	15.998 ± 0.026	16.019 ± 0.023	15.970 ± 0.037	15.986 ± 0.017	15.992 ± 0.127
15.980 ± 0.020	15.992 ± 0.024	16.011 ± 0.021	15.963 ± 0.030	15.980 ± 0.016	15.985 ± 0.114
16.250 ± 0.022	16.263 ± 0.027	16.284 ± 0.023	16.235 ± 0.035	16.251 ± 0.018	16.257 ± 0.127
16.272 ± 0.023	16.285 ± 0.027	16.307 ± 0.024	16.257 ± 0.147	16.273 ± 0.019	16.279 ± 0.241
17.313 ± 0.033	17.320 ± 0.038	17.331 ± 0.034	17.289 ± 0.051	17.306 ± 0.028	17.312 ± 0.186
17.319 ± 0.032	17.330 ± 0.036	17.348 ± 0.033	17.301 ± 0.046	17.318 ± 0.027	17.323 ± 0.176
17.954 ± 0.043	17.963 ± 0.048	17.980 ± 0.045	17.934 ± 0.062	17.951 ± 0.039	17.956 ± 0.239
18.500 ± 0.025	18.502 ± 0.028	18.507 ± 0.026	18.470 ± 0.030	18.488 ± 0.021	18.493 ± 0.133
19.123 ± 0.047	19.130 ± 0.051	19.141 ± 0.048	19.099 ± 0.056	19.117 ± 0.043	19.122 ± 0.246
19.096 ± 0.061	19.101 ± 0.065	19.109 ± 0.062	19.069 ± 0.070	19.087 ± 0.057	19.092 ± 0.317
19.916 ± 0.087	19.918 ± 0.092	19.924 ± 0.088	19.886 ± 0.098	19.905 ± 0.083	19.910 ± 0.451
24.901 ± 0.305	24.902 ± 0.312	24.905 ± 0.308	24.869 ± 0.340	24.888 ± 0.299	24.893 ± 1.565
20.402 ± 0.053	20.405 ± 0.057	20.410 ± 0.054	20.373 ± 0.058	20.391 ± 0.050	20.396 ± 0.274
20.810 ± 0.053	20.811 ± 0.056	20.814 ± 0.054	20.778 ± 0.058	20.797 ± 0.049	20.802 ± 0.272
21.286 ± 0.072	21.287 ± 0.075	21.290 ± 0.072	21.255 ± 0.077	21.273 ± 0.068	21.278 ± 0.365
21.074 ± 0.208	21.078 ± 0.212	21.085 ± 0.209	21.046 ± 0.216	21.065 ± 0.204	21.070 ± 1.051
21.870 ± 0.118	21.871 ± 0.121	21.874 ± 0.118	21.838 ± 0.122	21.857 ± 0.114	21.862 ± 0.595
22.536 ± 0.144	22.537 ± 0.147	22.541 ± 0.144	22.505 ± 0.149	22.524 ± 0.140	22.529 ± 0.726

Table 6: Apparent magnitudes of nova at sequential epochs along with the estimated uncertainties calculated using standard secondary stars.

Using the value of $M_{r'}^{t_2}$, $d_{t_2} = 857.43^{+366.62}_{-256.81}$ kpc.
Using the value of $M_{r'}^{t_3}$, $d_{t_3} = 657.66^{+432.78}_{-260.83}$ kpc.

The t_{15} relation by Ferrarese, Côté, & Jordán (2003) states that, the absolute magnitude of a nova, 15 days post maximum is given by,

$$M_V^{t_{15}} = -6.36 \pm 0.29 \tag{8}$$

Once again, if we assume that this relation holds true for r'-band magnitudes also, then using the value of $M_{r'}^{t_{15}}$, we estimate the distance to the nova as, $d_{t_{15}} = 835.60^{+119.39}_{-104.46}$ kpc.

2.2 Spectroscopy

To study the spectral evolution of the nova, the `splat` software is used, which is also a part of the Starlink suite of software applications. A spectrum is a plot of power per unit area, per unit wavelength (flux density) as a function of wavelength, which essentially tells us the distribution of energy as a function of wavelength. This is indicated by the units assigned to x and y-axes, *i.e.* erg s^{-1} cm^{-2} $Å^{-1}$ and Å, respectively, where an *erg* is a unit of energy, numerically equal to 10^{-7}Joules.

When a spectrum is viewed in the `splat` software, one can see and identify five major components in the spectral plot.

- Continuum emission from thermal radiations emitted over a large wavelength range by the inner dense material.
- Emission lines from radiation emitted by surrounding ejecta which absorbs wavelengths from continuum and emits at specific wavelengths.
- Absorption lines from radiation absorbed by the column of interstellar medium (ISM) in our line of sight of nova.

- Cosmic rays of galactic, extra-galactic and solar origins.
- Statistical noise inherent to measurements from instruments. Also called shot noise, it doesn't have any fixed pattern.

The most prominent of these features, the emission lines, are essentially the *recombination lines* formed when an ion captures a free electron. The electron is captured at higher energy levels of the ion and then *cascades* down to lower energy levels, thereby emitting at multiple wavelengths. The least prominent of all features, which require zooming in at specific wavelengths, are the ISM absorption lines that are formed due to absorption at specific wavelength by cold gas of extremely low density. Dust containing metals also absorbs certain wavelengths depending upon the metals contained in the grains. Statistical noise and Cosmic ray hits, on the other hand, are random features and differ in intensities and locations across different exposures randomly.

One thing to note is that at each epoch, three short exposures are obtained by the SPRAT module on Liverpool Telescope, instead of one (3x) long exposure. Although this has one disadvantage of slight increase in readout noise, there are several advantages which far outweigh the disadvantages. Multiple exposure prevent the saturation of CCD units by brightest features and can also be used to remove random defects. More importantly, the cosmic ray hits and transient bright objects in the sky (asteroids, satellites, etc.) can be easily located and handled accordingly.

Cosmic ray hits, which occur at random energies (wavelengths), can be removed from the spectra if multiple exposures are available by taking the median value at each point. This approach of median stacking, however, does not work for statistical noise, which is seen at every wavelength.

We can begin our spectral analysis by taking median value of three exposures at each epoch. The removal of cosmic ray hits can be observed once this is done following the procedure mentioned in the handout. We can then compare the time-evolution of the five components mentioned above, by observing trends across the 10 spectra now available to us.

- Continuum emission reduces in strength over time. The reduction is more prominent in the earlier spectra.
- Emission lines also reduce in strength over time more prominently in the earlier spectra. Some weaker emissions fade completely over time.
- ISM absorption is comparatively stronger when continuum emission is stronger. With passing time absorption fades.
- Cosmic ray hits remain constant, but their occurrence has been removed from spectra upon taking median for each epoch, given their insignificance in our study.
- Statistical noise appears to increase slightly as we go to later spectra. However, that appears due to reduction in value of SNR over time.

To summarize our work so far, we have used median stacking process for all 10 epochs using multiple exposures. This has removed cosmic ray signatures almost entirely, while statistical noise has not seen any major change. All other components have been preserved although extremely small signals may now seem lost in the statistical noise. We know now that the strength of continuum fades over time. Given that its presence is not much significant any further in our study, which comprises primarily of emission lines and ISM absorption lines, we can remove the continuum by fitting an approximate function that imitates its profile, and then subtract it from the spectrum. Such a spectrum is called a *continuum subtracted spectrum.* In our case, a polynomial of degree 3 gave the best improvement in reduction of root-mean-square error and was thus used to remove the continuum from spectra at each epoch. To ascertain whether the continuum has been appropriately subtracted, we repeat the procedure of continuum removal once again. This time, we get a continuum fitting curve which is a horizontal line corresponding to zero flux density, indicating that continuum

wavelength	continuum flux	line flux	EW	E(B–V)
5890.009 ± 0.061	$(2.400 \pm 0.1507) \times 10^{-16}$	$(-1.345 \pm 1.143) \times 10^{-16}$	0.560	0.199 ± 0.069
5895.935 ± 0.175	$(2.402 \pm 0.1507) \times 10^{-16}$	$(-0.931 \pm 1.263) \times 10^{-16}$	0.388	0.158 ± 0.062

Table 7: The values of central wavelength, continuum flux, absorption line flux, equivalent widths and interstellar reddening for the two sodium interstellar absorption lines.

has been successfully removed. Using a higher order polynomial for this purpose also gave insignificant fitting values.

A number of emission lines can new be easily recognized in each spectrum, some of which correspond to emissions from H I (H δ, H γ, H β, H α), Fe II (42,48,49), O I (1,21,55) and possibly Si II (4). Using classification provided by Williams (2012), we can conclude that nova is of Fe II spectroscopic class.

It is known that effects of interstellar extinction are prevalent over a continuous wavelength range. However, we can identify two interstellar absorption lines, which are collectively called the Na I doublet corresponding to wavelengths 5889.95Å (D2) and 5895.92Å (D1). By fitting Lorentzian line profiles to these two absorption lines, we can estimate the flux absorbed. The interstellar reddening E(B–V) can be calculated using the equations (Poznanski et al., 2012),

$$\log\left[E(B-V)\right] = 2.16 \times \mathrm{EW(D2)} - 1.91 \pm 0.15, \tag{9}$$

$$\log\left[E(B-V)\right] = 2.47 \times \mathrm{EW(D1)} - 1.76 \pm 0.17, \tag{10}$$

where, EW stands for *equivalent width* of corresponding lines, given by,

$$\mathrm{EW} \approx -\frac{F_{line}}{f_{cont}}, \tag{11}$$

where, F_{line} is the (negative) flux of absorption line and f_{cont} is the continuum flux at that wavelength. Using this procedure, the calculated values for the two absorption lines are summarized in table 7. The average value of reddening term computed from the two lines is given by E(B–V) $= 0.1785 \pm 0.093$.

While fitting the lines, three different types of line profiles are encountered – Gaussian, Lorentzian and Voigt. In this study, Lorentzian profile gave the best fit in all cases, with least root-mean-square errors. Voigt profile is essentially a convolution of the other two types of profiles.

In a similar manner, line fitting is performed for O I (7773Å) line and four Balmer lines, H δ (4102Å), H γ (4340Å), H β (4861Å) and H α (6563Å). The computed values of flux and full width half maximum (FWHM) are summarized in tables 8 and 9, respectively. Although the values of FWHM are mentioned in units of

O I (1)	$H\alpha$	$H\beta$	$H\gamma$	$H\delta$
$(1.96 \pm 0.01)10^{-13}$	$(4.95 \pm 0.02)10^{-13}$	$(7.58 \pm 0.07)10^{-14}$	$(3.18 \pm 0.04)10^{-14}$	$(2.08 \pm 0.03)10^{-14}$
$(2.98 \pm 0.03)10^{-14}$	$(2.75 \pm 0.01)10^{-13}$	$(4.08 \pm 0.06)10^{-14}$	$(1.88 \pm 0.04)10^{-14}$	$(1.50 \pm 0.04)10^{-14}$
$(1.55 \pm 0.01)10^{-14}$	$(1.70 \pm 0.00)10^{-13}$	$(2.49 \pm 0.04)10^{-14}$	$(1.09 \pm 0.02)10^{-14}$	$(8.93 \pm 0.29)10^{-15}$
$(1.12 \pm 0.01)10^{-14}$	$(1.27 \pm 0.00)10^{-13}$	$(1.85 \pm 0.03)10^{-14}$	$(8.25 \pm 0.20)10^{-15}$	$(6.12 \pm 0.20)10^{-15}$
$(7.30 \pm 0.35)10^{-15}$	$(8.41 \pm 0.06)10^{-14}$	$(1.19 \pm 0.03)10^{-14}$	$(5.50 \pm 0.38)10^{-15}$	$(2.74 \pm 0.40)10^{-15}$
$(6.70 \pm 0.41)10^{-15}$	$(7.87 \pm 0.05)10^{-14}$	$(1.08 \pm 0.02)10^{-14}$	$(5.51 \pm 0.42)10^{-15}$	$(2.39 \pm 0.81)10^{-15}$
$(5.83 \pm 0.53)10^{-15}$	$(7.23 \pm 0.05)10^{-14}$	$(1.00 \pm 0.02)10^{-14}$	$(3.80 \pm 0.46)10^{-15}$	$(2.25 \pm 4.81)10^{-15}$
$(5.88 \pm 1.15)10^{-15}$	$(7.25 \pm 0.06)10^{-14}$	$(1.01 \pm 0.03)10^{-14}$	$(4.47 \pm 0.29)10^{-15}$	$(5.71 \pm 6.09)10^{-15}$
$(6.59 \pm 1.15)10^{-15}$	$(7.07 \pm 0.06)10^{-14}$	$(9.50 \pm 0.31)10^{-15}$	$(5.09 \pm 0.63)10^{-15}$	$(2.57 \pm 1.08)10^{-15}$
$(5.21 \pm 1.52)10^{-15}$	$(6.77 \pm 0.06)10^{-14}$	$(9.14 \pm 0.27)10^{-15}$	$(4.74 \pm 0.38)10^{-15}$	$(4.12 \pm 69.0)10^{-15}$

Table 8: Fluxes and associated uncertainties obtained for different emission lines (in units of erg s^{-1} cm^{-2} $Å^{-1}$) across spectra at all epochs, mentioned sequentially. Values are truncated at two decimal places for representational purpose.

O I (1)	$H\alpha$	$H\beta$	$H\gamma$	$H\delta$
78.714 ± 0.634	51.444 ± 0.219	47.185 ± 0.393	51.671 ± 0.620	51.791 ± 0.723
54.016 ± 0.461	34.377 ± 0.129	32.503 ± 0.395	40.518 ± 0.826	46.489 ± 1.218
40.734 ± 0.431	25.816 ± 0.107	24.359 ± 0.347	27.682 ± 0.525	33.247 ± 0.947
34.328 ± 0.425	21.706 ± 0.097	20.642 ± 0.335	24.232 ± 0.518	25.271 ± 0.750
27.558 ± 1.143	18.785 ± 0.120	17.328 ± 0.367	21.666 ± 1.342	12.441 ± 1.722
28.294 ± 1.528	18.681 ± 0.110	16.260 ± 0.368	22.766 ± 1.578	12.364 ± 4.088
27.210 ± 2.297	18.759 ± 0.114	16.619 ± 0.381	15.875 ± 1.816	12.843 ± 27.378
27.340 ± 5.240	18.760 ± 0.129	16.319 ± 0.445	19.282 ± 1.116	34.943 ± 37.214
33.103 ± 5.612	18.822 ± 0.133	16.453 ± 0.458	23.854 ± 2.776	15.605 ± 6.468
25.836 ± 7.491	18.884 ± 0.138	16.123 ± 0.404	23.214 ± 1.677	8.028 ± 33.176

Table 9: FWHM and associated uncertainties obtained for different emission lines (in units of Å) across spectra at all epochs, mentioned sequentially.

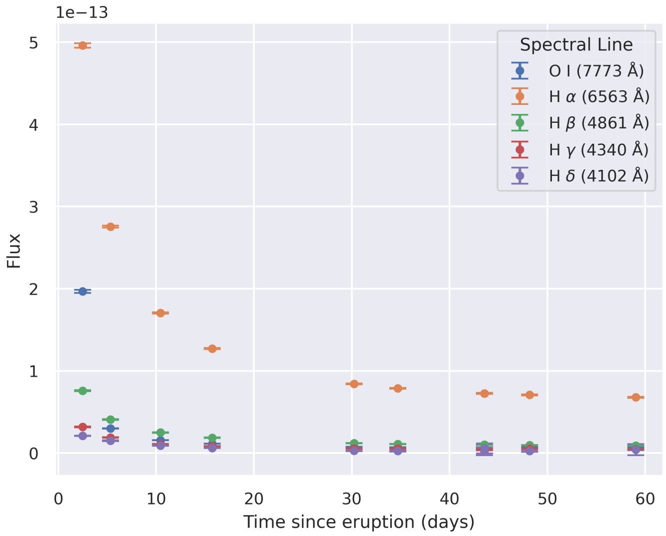

(a) Time evolution of flux (in erg s^{-1} cm^{-2} Å^{-1}) of spectral lines.

(b) Time evolution of flux ratios of spectral lines.

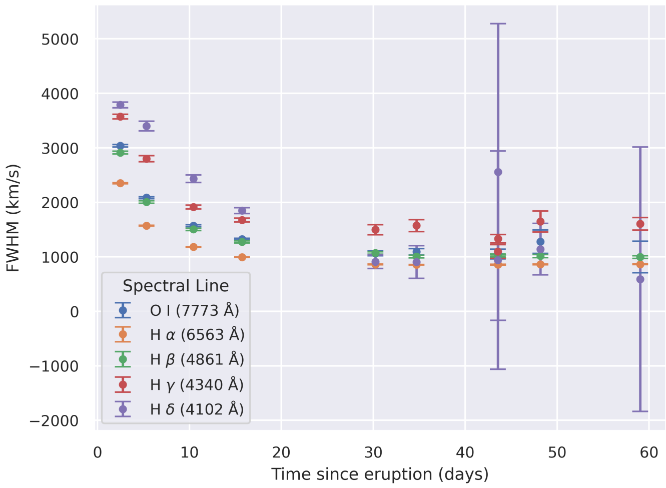

(c) Time evolution of FWHM (in units of km s^{-1}) of spectral lines.

Figure 2: Evolution of parameters derived from the analysis of spectroscopic images obtained over the course of $\sim 60 days$.

wavelength change, *i.e.* Å, this is not the typical unit of representation. The values are often represented in units of velocity (km s^{-1}) because the span of a spectral line, quantified by FWHM is a function of velocity of the material emitting at the given wavelength. These units therefore help us understand the morphology and kinematics of the ejected material emitting at those wavelengths.

The evolution of line fluxes, line flux ratios and line widths are shown in figures 2a, 2b and 2c respectively.

If we plot the graphs in figure 2 on log-log plots, we can easily realise that all these evolutions can be described by simple power-law relations. As time evolves, nova ejecta is slowed down eventually as it reaches and collides with the circum-stellar material ejected by the star while it was still evolving. This slow down of velocity is evident from the time evolution of FWHM in units of velocity in figure 2c

From the values of the ten employed continuum fits, it can be inferred that as the system evolves the overall value of the continuum across all wavelengths decreases. Continuum contribution in the blue wavelengths begins to dominate than in redder wavelengths as time evolves, and therefore, the colour of the nova tends towards blue as time evolves. Absolute magnitude value is estimated using photometry in section 2.1 and is of the order of ~ -8 magnitudes. This is a fairly typical value for a classical nova.

Using the equation,

$$A_{r'} = 2.751 \times \text{E(B-V)},$$

we obtain a value of $A_{r'} = 0.491 \pm 0.256$. This value can be used in equation 7 to improve our estimate of distance of nova. Using equations 5, 6 and 8, we obtain the following distance estimates.

$$d_{t_2} = 683.282^{+413.701}_{-257.683}\text{kpc},$$

$$d_{t_3} = 524.807^{+453.780}_{-243.358}\text{kpc},$$

$$d_{t_{15}} = 666.806^{+190.231}_{-148.006}\text{kpc}.$$

Based on these distance estimates, The most probable location of the classical nova seems to be in M31 galaxy (Riess, Fliri, & Valls-Gabaud, 2012).

References

Dovi Poznanski, J. Xavier Prochaska, Joshua S. Bloom, An empirical relation between sodium absorption and dust extinction, Monthly Notices of the Royal Astronomical Society, Volume 426, Issue 2, 21 October 2012, Pages 1465–1474, https://doi.org/10.1111/j.1365-2966.2012.21796.x

Strope R. J., Schaefer B. E., Henden A. A., 2010, AJ, 140, 34. doi:10.1088/0004-6256/140/1/34

Tonry J. L., Stubbs C. W., Lykke K. R., Doherty P., Shivvers I. S., Burgett W. S., Chambers K. C., et al., 2012, ApJ, 750, 99. doi:10.1088/0004-637X/750/2/99

Williams R., 2012, AJ, 144, 98. doi:10.1088/0004-6256/144/4/98

Downes R. A., Duerbeck H. W., 2000, AJ, 120, 2007. doi:10.1086/301551

Darnley M. J., Bode M. F., Kerins E., Newsam A. M., An J., Baillon P., Belokurov V., et al., 2006, MNRAS, 369, 257. doi:10.1111/j.1365-2966.2006.10297.x

Riess A. G., Fliri J., Valls-Gabaud D., 2012, ApJ, 745, 156. doi:10.1088/0004-637X/745/2/156

Ferrarese L., Côté P., Jordán A., 2003, ApJ, 599, 1302. doi:10.1086/379349